Liquid pumping induced by transverse forced vibrations of an elastic beam: A lubrication approach

Rodica Borcia* and Michael Bestehorn
Chair of Statistical Physics and Nonlinear Dynamics, Brandenburg University of Technology, Cottbus-Senftenberg, 03046 Cottbus, Germany

Sebastian Uhlig, Matthieu Gaudet, and Harald Schenk
Chair Micro- and Nanosystems, Brandenburg University of Technology, Cottbus-Senftenberg, 03046 Cottbus, Germany
and Fraunhofer Institute for Photonic Microsystems, ISS, Cottbus, 03046 Cottbus, Germany

(Received 31 January 2018; published 20 August 2018; corrected 19 February 2019)

Two liquid pumps are investigated theoretically and numerically: a single thin liquid layer actuated by a periodic force at an elastic beam and a two-layer geometry actuated by an elastic beam. For the second geometry, the beam actuates the liquid from both sides. For both pumps, the liquid film thickness is small compared to the lateral characteristic length of the system. A lubrication theory is developed. The Euler-Bernoulli equation for transverse deformations of an elastic beam is coupled to the fundamental hydrodynamic equations: the Navier-Stokes equation and a continuity equation in the long-wave approximation. In this way, one connects the transverse displacement of the beam with the hydrodynamic quantities (pressure, velocity fields, and flow rates). Appropriate boundary conditions incorporate the function of the valves. The derivation of the theoretical model is followed by numerical simulations. We estimate flow rates (in two and three spatial dimensions) for different system parameters and we compute the efficiency of a well-designed liquid pump.

DOI: 10.1103/PhysRevFluids.3.084202

I. INTRODUCTION

The behavior of liquid thin films is of great importance for technological applications such as oil recovery, inkjet printing, emulsion stability or control in micro- and nanofluidics, actuators, and micropumps (see Refs. [1–8] and references therein). Micropumps have a large range of potential use in microelectromechanical systems, especially in biological and medical fields such as pressure sensors in cardiac implanted devices, human retinal prosthesis, or tactile sensing [9].

For thin liquid films, the most simple and suitable mathematical model which still captures the main physics is the lubrication approximation known also as long-wave theory, valid for a mean liquid thickness d much smaller than the lateral characteristic length of the liquid film L, so that the aspect ratio δ defined as $\delta = d/L$ is much smaller than one. This approach is based on the asymptotic reduction of the full set of basic hydrodynamic equations and boundary conditions to a simplified system which consists of a single partial differential equation describing the spatiotemporal evolution of the local thickness of the liquid film. Expanding the velocity and pressure fields in powers of the small parameter δ and enslaving the velocity by the film thickness, one may deduce the standard thin-film equation from the zeroth-order problem in δ (see Refs. [10,11] and references therein). The lubrication approximation allows for a reduction of three-dimensional (3D)

*borciar@b-tu.de

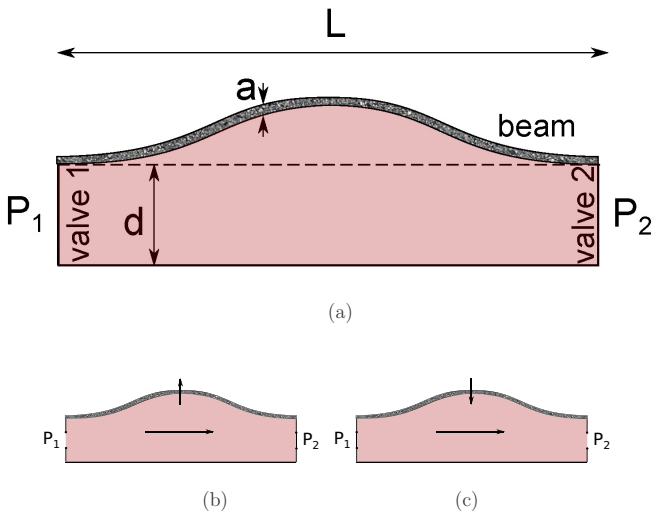

FIG. 1. (a) Schematic representation of a liquid micropump actuated at the upper boundary by an elastic beam, fixed at the ends. The bottom boundary is a rigid impermeable plate. Laterally, the system is equipped with two valves, valve 1 on the left side and valve 2 on the right side, which can establish the connection with two reservoirs with pressures P_1 and P_2. Also shown is the schematic of the temporal cycle: (b) first half-time and (c) second half-time.

problems to a 2D description in two horizontal coordinates. This drastically reduces the computing time, making this method very convenient and attractive for numerical simulations of thin liquid films.

The lubrication approach showed in the past considerable success in modeling long-wave Marangoni convection induced by thermal effects in one-layer systems, stability of thin films under gravity effects, structure formation [12–15], sliding drops on slightly sloped planes with small contact angles [16,17], 3D drops, and also rivulet stability on homogeneous and heterogeneous substrates with and without inclination [18–20]. Not only common liquids, but also liquid binary mixtures with miscible components have been widely studied in the past decade in the frame of long-wave theory [21–28]. Recent works on inertial lubrication approximation reported the role of external vibrations (at the solid bottom boundary) on one- or two-layer liquid systems [29–36]. Thus, stability and instability phenomena, pattern formation, force-driven flows, ratchet systems, coupling (interaction) of modes, and drop motion control under vibrations were explored.

The present paper presents a lubrication approach, a mathematical tool suitable for describing the fluid dynamics in micropumps induced by transverse forced vibrations of an elastic beam. The paper is organized as follows. Section II gives the derivation of the model equations for a micropump in one-layer geometry in two spatial dimensions and the linear stability analysis. Stationary- and time-dependent problems are also discussed here. Section III presents the extension of the model for a two-layer geometry as well as the extension in the third spatial dimension. We will show how the valves can be incorporated (realizing in this way a ratchet system), consider a porous elastic beam, and finally compute physical quantities of interest for pumps such as flow rate, fluidic (power) work, and pump efficiency. We summarize in Sec. IV.

II. TWO-DIMENSIONAL LUBRICATION THEORY: ONE-LAYER GEOMETRY

A. Derivation of the model: Linear stability analysis

We assume a liquid film actuated at the upper side by an elastic beam, fixed at the ends, as sketched in Fig. 1. Initially, the system is at rest on a rigid (impermeable) plate placed at $z = 0$. The transverse

deformation in an elastic beam obeys the Euler-Bernoulli equation [8,37,38]

$$\rho_A ab\frac{\partial^2\tilde{\eta}}{\partial\tilde{t}^2} + EI\frac{\partial^4\tilde{\eta}}{\partial\tilde{x}^4} = -b(\tilde{p}_A - \tilde{p}), \tag{1}$$

where $\tilde{\eta}$ designates the deflection of the upper boundary (the transverse displacement of the beam), ρ_A the beam density, E the Young (elastic) modulus, and I the second moment of area of the beam's cross section. For a rectangular cross section having thickness a and depth b, the second moment of the area is $I = ba^3/12$. In Eq. (1) (written per unit length of the beam), the first term on the left-hand side describes the inertial effects, the second one emphasizes the contribution of the internal (elastic) forces, and the damping effects inside the beam are neglected. The terms on the right-hand side of (1) describe the contribution of the external forces at the actuator, expressed in pressure terms. On one side we have the externally applied pressure (for example, caused by electrostatic forces) $\tilde{p}_A$ and on the other side the liquid pressure. The pressure field of the liquid $\tilde{p}$ couples Eq. (1) coming from the vibration theory with the fundamental equations of hydrodynamics. We start from the two-dimensional incompressible Navier-Stokes equations

$$\frac{\partial\tilde{v}_x}{\partial\tilde{t}} + \tilde{v}_x\frac{\partial\tilde{v}_x}{\partial\tilde{x}} + \tilde{v}_z\frac{\partial\tilde{v}_x}{\partial\tilde{z}} = -\frac{1}{\rho}\frac{\partial\tilde{p}}{\partial\tilde{x}} + \nu\left(\frac{\partial^2\tilde{v}_x}{\partial\tilde{x}^2} + \frac{\partial^2\tilde{v}_x}{\partial\tilde{z}^2}\right), \tag{2}$$

$$\frac{\partial\tilde{v}_z}{\partial\tilde{t}} + \tilde{v}_x\frac{\partial\tilde{v}_z}{\partial\tilde{x}} + \tilde{v}_z\frac{\partial\tilde{v}_z}{\partial\tilde{z}} = -\frac{1}{\rho}\frac{\partial\tilde{p}}{\partial\tilde{z}} + \nu\left(\frac{\partial^2\tilde{v}_z}{\partial\tilde{x}^2} + \frac{\partial^2\tilde{v}_z}{\partial\tilde{z}^2}\right) \tag{3}$$

and the continuity equation

$$\frac{\partial\tilde{v}_x}{\partial\tilde{x}} + \frac{\partial\tilde{v}_z}{\partial\tilde{z}} = 0, \tag{4}$$

with the boundary conditions

$$\tilde{v}_x|_{\tilde{z}=0} = \tilde{v}_z|_{\tilde{z}=0} = 0, \tag{5}$$

$$\vec{\tilde{v}}\cdot\vec{\tilde{n}}|_{\text{beam}} = \frac{\partial\tilde{\eta}}{\partial\tilde{t}}, \quad \vec{\tilde{v}}\cdot\vec{\tilde{t}}|_{\text{beam}} = 0, \tag{6}$$

ν being the kinematic viscosity, and $\vec{\tilde{n}}$ and $\vec{\tilde{t}}$ the normal and the tangential vectors at the deflected beam

$$\vec{\tilde{n}} = \frac{1}{\sqrt{1+\left(\frac{\partial\tilde{\eta}}{\partial\tilde{x}}\right)^2}}\begin{pmatrix}-\frac{\partial\tilde{\eta}}{\partial\tilde{x}}\\ 1\end{pmatrix}, \quad \vec{\tilde{t}} = \frac{1}{\sqrt{1+\left(\frac{\partial\tilde{\eta}}{\partial\tilde{x}}\right)^2}}\begin{pmatrix}1\\ \frac{\partial\tilde{\eta}}{\partial\tilde{x}}\end{pmatrix}.$$

We consider the long-wave approximation $\delta = d/L \ll 1$, where d represents the mean thickness of the liquid film and L is the lateral length of the micropump. We scale the problem as follows:

$$\tilde{x} = xL, \quad \tilde{z} = zd, \quad \tilde{\eta} = \eta d, \quad \tilde{t} = t\frac{d^2}{\nu},$$

$$\tilde{v}_x = v_x\frac{L\nu}{d^2}, \quad \tilde{v}_z = v_z\frac{\nu}{d}, \quad \tilde{p} = p\frac{\rho L^2\nu^2}{d^4}.$$

The above scaling does not belong to standard lubrication theories presented in Refs. [10,11]. Our scaling belongs to inertial lubrication theory (see, for example, Ref. [31]), capturing also the inertial effects in the mathematical model.

After scaling Eqs. (2)–(6) we find, in the zeroth order δ^0 (and neglecting all the nonlinearities),

$$\frac{\partial v_x}{\partial t} = -\frac{\partial p}{\partial x} + \frac{\partial^2 v_x}{\partial z^2}, \tag{7}$$

$$\frac{\partial p}{\partial z} = 0, \tag{8}$$

$$\frac{\partial v_x}{\partial x} + \frac{\partial v_z}{\partial z} = 0, \tag{9}$$

$$v_x|_{z=0} = 0, \quad v_z|_{z=0} = 0, \tag{10}$$

$$\frac{\partial \eta}{\partial t} = v_z|_{z=1+\eta} - v_x|_{z=1+\eta}\frac{\partial \eta}{\partial x}, \tag{11}$$

$$v_x|_{z=1+\eta} = 0. \tag{12}$$

Using (9), Eq. (11) can be written in the conservative form

$$\frac{\partial \eta}{\partial t} = -\frac{\partial q}{\partial x}, \tag{13}$$

with $q(x,t) = \int_0^{1+\eta} v_x dz$ the mass flux (flow rate) per unit length. This condition constitutes a more convenient form of the kinematic condition (11) and ensures the conservation of mass on a domain with a deflecting upper boundary.

From Eq. (8) we can can deduce that the pressure p depends only on x coordinate. Making use of the no-slip boundary conditions (10) and (12), we assume v_x as a Hagen-Poiseuille flow [34]

$$v_x(x,z,t) = Az(1+\eta-z).$$

Substituting the above ansatz into the flow rate, we obtain

$$A = \frac{6q}{(1+\eta)^3}.$$

Integrating Eq. (7) in the z direction between 0 and $1+\eta$, we arrive at

$$\frac{\partial q}{\partial t} = -(1+\eta)\frac{\partial p}{\partial x} - \frac{12q}{(1+\eta)^2}. \tag{14}$$

Thus, we have derived a closed system of (1), (13), and (14) for the variables η, q, and p, which reads

$$\frac{\partial^2 \eta}{\partial t^2} + \alpha\frac{\partial^4 \eta}{\partial x^4} = -\beta(p_A - p), \tag{15}$$

$$\frac{\partial \eta}{\partial t} = -\frac{\partial q}{\partial x}, \tag{16}$$

$$\frac{\partial p}{\partial x} = -\frac{12q}{(1+\eta)^3} - \frac{1}{(1+\eta)}\frac{\partial q}{\partial t}, \tag{17}$$

with the parameters $\alpha = \frac{Ea^2d^4}{12\rho_A\nu^2L^4}$ and $\beta = \frac{\rho L^2}{\rho_A da}$.

Performing in the above system of equations a linear stability analysis for the case without driving $p_A = 0$ around the fixed point $\eta^{(0)} = q^{(0)} = p^{(0)} = 0$, assuming for the small perturbations plane waves in the horizontal direction

$$\begin{pmatrix} \eta^{(1)}(x,t) \\ q^{(1)}(x,t) \\ p^{(1)}(x,t) \end{pmatrix} = \begin{pmatrix} \eta^* \\ q^* \\ p^* \end{pmatrix} \exp(ikx)\exp(\lambda t),$$

where k denotes the wave number, λ is the (complex) growth rate of the instability, and η^*, q^*, and p^* are complex amplitudes, we get, for the solutions of the characteristic equation,

$$\lambda_{1,2} = \frac{-6\beta \pm \sqrt{36\beta^2 - \alpha k^6(\beta + k^2)}}{\beta + k^2}.$$

Both solutions have $\mathrm{Re}(\lambda) < 0$, i.e., the fixed point $\eta^{(0)} = q^{(0)} = p^{(0)} = 0$ is linearly stable for all k.

B. Stationary problem

Now the beam is deformed by two couples of forces acting at the actuator, given by p_A. For the stationary problem, the system (15)–(17) reduces only to the stationary Euler-Bernoulli equation

$$\alpha \frac{d^4\eta}{dx^4} = -\beta p_A. \tag{18}$$

To solve (18), we apply a finite-difference method on a uniform grid with N intervals and the grid size $\Delta x = 1/N$ [39–41]. The beam is fixed at the ends. Thus, we assume as boundary conditions

$$\eta(0) = \eta(N) = 0, \quad d\eta/dx|_0 = d\eta/dx|_N = 0.$$

It remains to solve an inhomogeneous linear system

$$A\vec{\eta} = B, \tag{19}$$

where

$$\vec{\eta} = \begin{pmatrix} \eta(1) \\ \eta(2) \\ \vdots \\ \vdots \\ \vdots \\ \eta(N-1) \end{pmatrix}$$

is the beam deformation vector discretized on the $N-1$ mesh points,

$$A = \begin{pmatrix} 7 & -4 & 1 & 0 & 0 & \cdots & \cdots & \cdots & \cdots & \cdots & 0 \\ -4 & 6 & -4 & 1 & 0 & \ddots & \ddots & \ddots & \ddots & \ddots & \vdots \\ 1 & -4 & 6 & -4 & 1 & \ddots & \ddots & \ddots & \ddots & \ddots & \vdots \\ \vdots & \ddots & \ddots & \ddots & \ddots & \ddots & \ddots & \ddots & \ddots & \ddots & \vdots \\ \vdots & \ddots & \ddots & \ddots & \ddots & \ddots & 1 & -4 & 6 & -4 & 1 \\ \vdots & \ddots & \ddots & \ddots & \ddots & \ddots & 0 & 1 & -4 & 6 & -4 \\ 0 & \cdots & \cdots & \cdots & \cdots & \cdots & 0 & 0 & 1 & -4 & 7 \end{pmatrix}$$

is an $(N-1) \times (N-1)$ band matrix, and $B(j) = 0$ except for four nonzero components representing the actuated pressure at the elastic beam: $B(N/4-1) = -\beta p_A \Delta x^4/\alpha$, $B(N/4+1) = \beta p_A \Delta x^4/\alpha$, $B(3N/4-1) = \beta p_A \Delta x^4/\alpha$, and $B(3N/4+1) = -\beta p_A \Delta x^4/\alpha$. The 7's in the corners of the matrix A appear from the second-order central difference formula

$$\frac{\eta_{i+2} - 4\eta_{i+1} + 6\eta_i - 4\eta_{i-1} + \eta_{i-2}}{\Delta x^4} = -\frac{\beta}{\alpha} p_A$$

applied for the components $\eta(1)$ and $\eta(N-1)$, taking into account the discretized boundary conditions $\eta(1) = \eta(-1)$ and $\eta(N+1) = \eta(N-1)$.

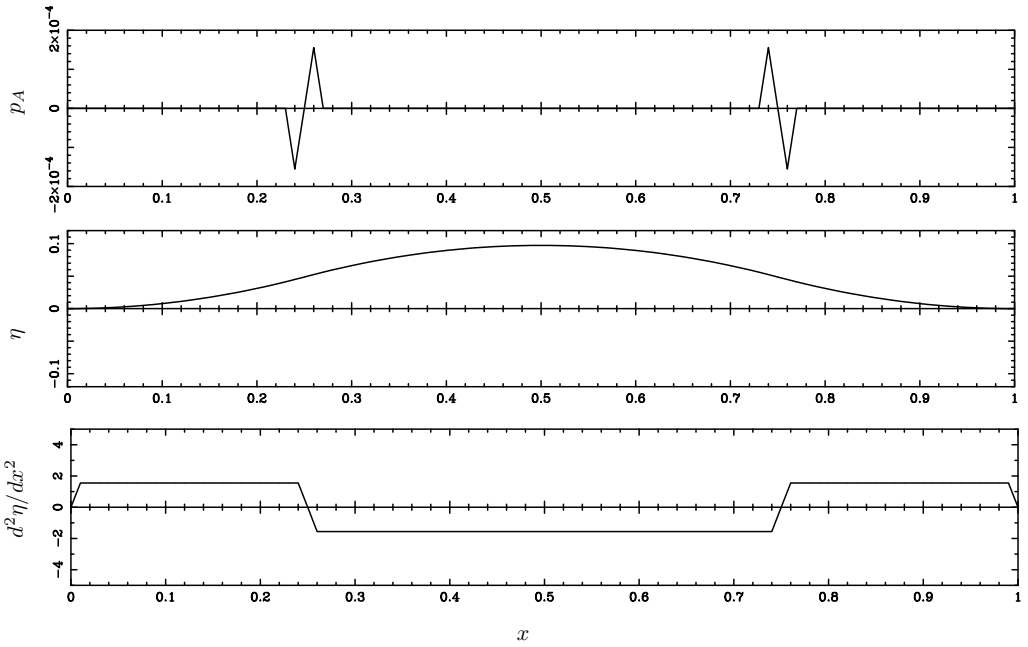

(a)

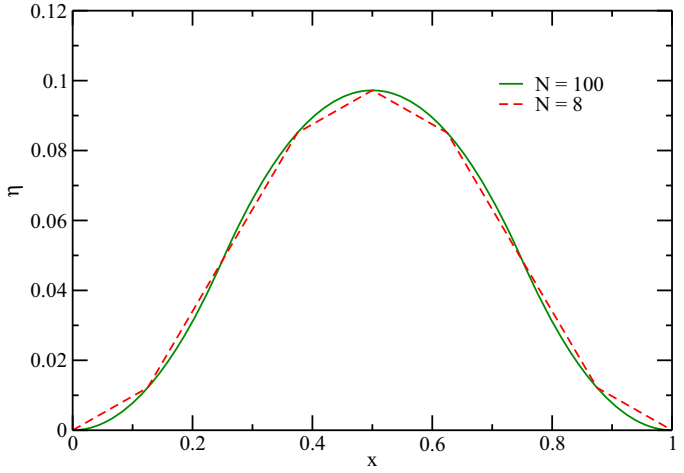

(b)

FIG. 2. Deformation of an elastic beam for the stationary problem. (a) Actuated pressure along the beam p_A for $N = 100$, the corresponding beam deformation η, and the second derivative of the beam deflection $d^2\eta/dx^2$. (b) Beam deformations for two different discretizations, showing the same maxima (of 7.3 μm) for $p_A = 30.8N^2$. The other parameters are $L = 1$ mm, $a = 10$ μm, $d = 75$ μm, $\rho = 10^3$ kg/m^3, $\nu = 10^{-6}$ m^2/s, $\rho_A = 2.336 \times 10^3$ kg/m^3, and $E = 10^{11}$ N/m^2.

The system (19) is solved by standard routines. We take the parameters for a water pump with a silicon elastic beam having $L = 1$ mm, $a = 10$ μm, $d = 75$ μm, $\rho = 10^3$ kg/m^3, $\nu = 10^{-6}$ m^2/s, $\rho_A = 2.336 \times 10^3$ kg/m^3, and $E = 10^{11}$ N/m^2, which leads to the model parameters $\alpha = 112.87 \times 10^2$ and $\beta = 570.77$.

The load at the actuator is distributed as shown in the top panel of Fig. 2(a). Two couples of forces act along the beam. Each couple of forces creates a torque about the zeroth of the second derivative of the deflected elastic beam $d^2\eta/dx^2$ [see Fig. 2(a)]. Assuming the actuated pressure $p_A = 30.8N^2$ ensures the same loading moment on the elastic beam, creating a maximal deformation of $\tilde{\eta}_{\max} = 7.3$ μm, independently of the number of the mesh points [as one can see from Fig. 2(b)]. For a smooth variation along the deformed elastic beam, in the following we set $N = 100$ ($\Delta x = 0.01$).

C. Time-dependent problem

For the time-dependent problem, we consider the same parameters as in the preceding section. The loading forces at the actuator vary periodically in time according to $p_A^{(j)}\sin^2(2\pi f t)$ (with $f =$ 200 Hz, i.e., the excitation frequency at the string $2f = 400$ Hz) acting at, respectively, $j = N/4 - 1, N/4 + 1, 3N/4 - 1, 3N/4 + 1$.

We solve (15)–(17) numerically in the following way. We choose the time step size small enough to ensure the independence of the results from the time integration. For each time step we solve (15), as presented in the precedent section. For the discretization of the temporal derivatives, we use the explicit Euler method and q is computed from (16) with $q(t, N) = 0$, with valve 1 open and valve 2 closed [Fig. 1(b)], and $q(t, 0) = 0$, with valve 1 closed and valve 2 open [Fig. 1(c)]. The pressure field at $t + \Delta t$ follows from (17) with $p(t, 0) = P_1$, with valve 1 open and valve 2 closed, and $P(t, N) = P_2$, with valve 1 closed and valve 2 open (with $P_1 < P_2$ for the device from Fig. 1 working in the pump regime). We set $P_1 = 200$ ($\tilde{P}_1 = 0.63 \times 10^4$ N/m^2) and $P_2 = 300$ ($\tilde{P}_2 = 0.95 \times 10^4$ N/m^2). For each time step, the three coupled equations are solved by iterative loops, until the relative errors for computing $\eta(x, t + \Delta t)$ fall below a certain fixed accuracy: $|\eta(t + \Delta t) - \eta(t)|/\eta(t) < 10^{-12}$. This results in 15–20 iterations loops per time step.

The facility presented in Fig. 1 pumps the liquid from the reservoir with lower pressure, with the time period $T = 0.44$ ($\tilde{T} \cong 2.5 \times 10^{-3}$ s). One micropump cycle consists of two half-times. During the first half-time, the elastic beam, initially (at $t = 0$) horizontal, moves (due to the actuated forces) in the upper direction. Valve 1 is open and valve 2 is closed. The liquid is pumped from the reservoir with the liquid pressure P_1. The maximum of the flowing rate is achieved at $t = 0.12$. When the deformation of the beam reaches its maximum, the flow rate inside the channel is almost zero. When the beam starts to move down, a return flow occurs in the micropump channel. In this moment valve 1 closes and valve 2 opens and the second half-time starts. The liquid is now pumped out to the reservoir with the pressure P_2. The pump reaches its flow rate maximum at $t = 0.34$. After that the flow rate decreases to zero and the elastic beam returns to the horizontal position. When the actuated beam starts again to deform in the upper direction, a return flows again occurs in the system. Therefore, valve 1 opens and valve 2 closes and in this way a new cycle of the pump begins. Figure 3 presents time series (during one complete period) of beam deformation and flow rate distribution along the micropump channel from the first half-time, with valve 1 open and valve 2 closed [Figs. 3(a) and 3(b)], and from the second half-time of the micropump, with valve 1 closed and valve 2 open [Figs. 3(c) and 3(d)]. The maximal flow rate achieved for the water micropump with the parameters mentioned in Sec. II B is 4.6×10^{-6} m^2/s.

III. EXTENSION TO THREE SPATIAL DIMENSIONS AND A TWO-LAYER SYSTEM

A. Derivation of the model

A sketch of the two-layer pump under consideration is shown in Fig. 4. For the moment, the system is assumed to be closed. The elastic beam actuates the liquid from both sides. The beam is fixed at the ends. At $x = 1$ the presence of an orifice permits the liquid to flow from the lower layer to the upper layer and vice versa.

We also take into account the depth of the channel b (namely, the third spatial dimension) and we use a Hagen-Poiseuille ansatz for the velocity profile v_x parabolically in both the z and y directions,

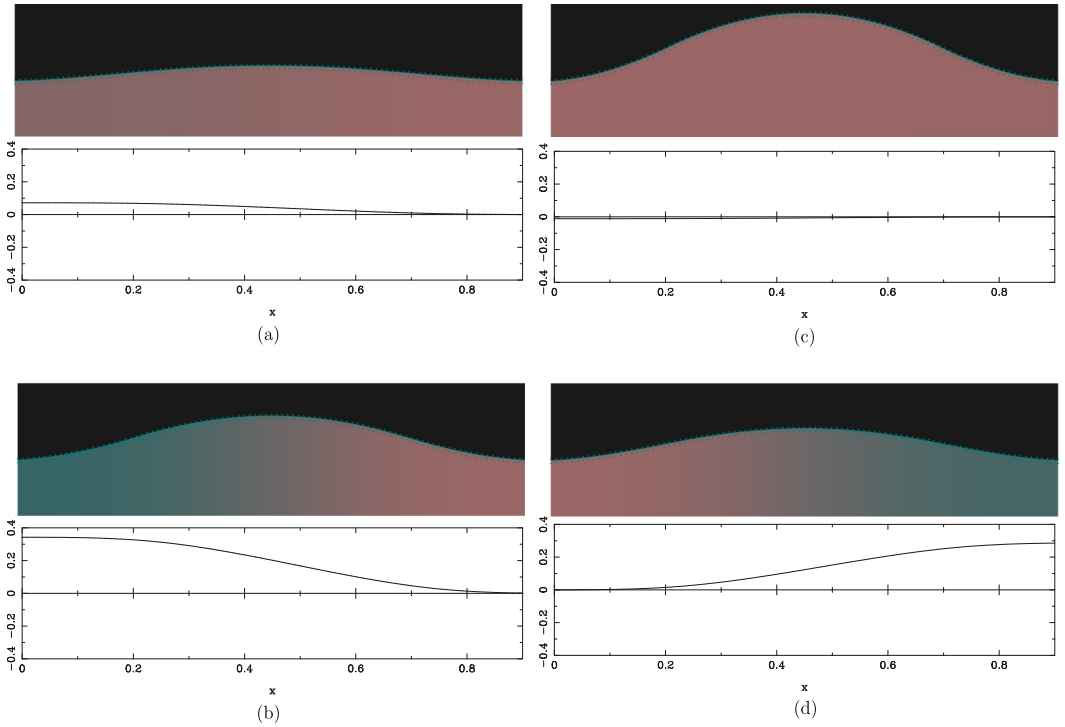

FIG. 3. Beam deformation and liquid flux rates (distributions along the pump channel) at different times, resulting from numerical simulations in two spatial dimensions: (a) $t = 0.04$, (b) $t = 0.12$, (c) $t = 0.23$, and (d) $t = 0.36$. The upper panels display also flow rate distributions by colors ranging from green for maxima to salmon pink for minima.

fulfilling no-slip conditions at $y = 0$ and $y = \delta_y$,

$$v_x(x, y, t) = Bz(1 + \eta - z)y(\delta_y - y), \tag{20}$$

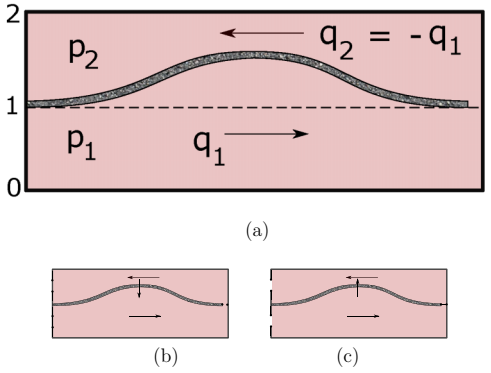

FIG. 4. (a) Schematic representation of a two-layer micropump. The elastic beam actuates now the liquid from both sides. The beam is fixed at the ends. At $x = 1$ the presence of an orifice permits the liquid to flow from the lower layer to the upper layer and vice versa. Also shown is the schematic of the temporal cycle after the implementation of the valves: (b) first half-time and (c) second half-time.

with $\delta_y = b/L$. Substituting (20) into the total flow rate

$$q = \int_0^{\delta_y} \int_0^{1+\eta} v_x dy\, dz,$$

we find

$$B = \frac{36q}{\delta_y^3(1+\eta)^3}.$$

By integrating the Navier-Stokes equation

$$\frac{\partial v_x}{\partial t} = -\frac{\partial p}{\partial x} + \frac{\partial^2 v_x}{\partial x^2} + \delta^2 \frac{\partial^2 v_x}{\partial y^2} \tag{21}$$

in the z direction between 0 and $1+\eta$ and in the y direction between 0 and δ_y, we get, for the 3D problem,

$$\frac{1}{\delta_y}\frac{\partial q}{\partial t} = -(1+\eta)\frac{\partial p}{\partial x} - \frac{12q}{\delta_y}\left[\frac{1}{(1+\eta)^2} + \frac{\delta^2}{\delta_y^2}\right]. \tag{22}$$

From the last term on the right-hand side we can see that the third spatial dimension becomes significant for $\delta^2/\delta_y^2 \gg 1$.

We apply the Euler-Bernoulli equation for the two-layer system

$$\frac{\partial^2 \eta}{\partial t^2} + \alpha \frac{\partial^4 \eta}{\partial x^4} = -\beta(p_A - p_1 + p_2) \tag{23}$$

and the mass conservation law twice for the lower and the upper side of the fluid, respectively,

$$\frac{\partial \eta}{\partial t} = -\frac{\partial q_1}{\partial x}\frac{1}{\delta_y}, \tag{24}$$

$$\frac{\partial \eta}{\partial t} = \frac{\partial q_2}{\partial x}\frac{1}{\delta_y}. \tag{25}$$

The subscripts 1 and 2 denote the pressure (and flow rate) in the lower and the upper side of the liquid, as can be seen from Fig. 4. Subtracting (25) from (24) and using one of the boundary conditions $q_1(t,0) = -q_2(t,0) = 0$ or $q_1(t,1) = -q_2(t,1) = 0$, we deduce that $q_1 = -q_2 = q$.

We apply the integrated Navier-Stokes equation (22) for the thin liquid layers with the heights $1+\eta$ and $1-\eta$, leading to, respectively,

$$\frac{1}{\delta_y}\frac{\partial q_1}{\partial t} = -(1+\eta)\frac{\partial p_1}{\partial x} - \frac{12q_1}{\delta_y}\left[\frac{1}{(1+\eta)^2} + \frac{\delta^2}{\delta_y^2}\right], \tag{26}$$

$$\frac{1}{\delta_y}\frac{\partial q_2}{\partial t} = -(1-\eta)\frac{\partial p_2}{\partial x} - \frac{12q_2}{\delta_y}\left[\frac{1}{(1-\eta)^2} + \frac{\delta^2}{\delta_y^2}\right]. \tag{27}$$

Multiplying (26) with $1/(1+\eta)$ and (27) with $1/(1-\eta)$ and subtracting the obtained equations, we get the spatial evolution equation of $\Delta P = p_1 - p_2$,

$$\begin{aligned}\frac{\partial(\Delta p)}{\partial x} = &-\frac{\partial q}{\partial t}\frac{1}{\delta_y}\left(\frac{1}{1+\eta} + \frac{1}{1-\eta}\right) \\ &- \frac{12q}{\delta_y}\left[\frac{1}{(1+\eta)^3} + \frac{1}{(1-\eta)^3} + \frac{\delta^2}{\delta_y^2}\frac{1}{1+\eta} + \frac{\delta^2}{\delta_y^2}\frac{1}{1-\eta}\right].\end{aligned} \tag{28}$$

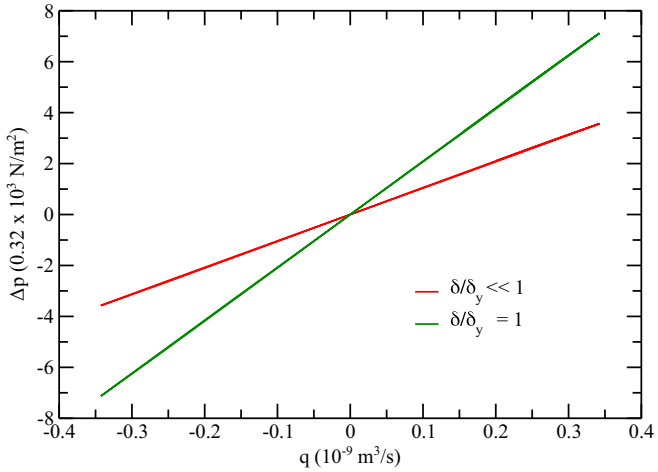

FIG. 5. Pressure difference $\Delta P = p_1 - p_2$ in the middle of the channel versus flow rate q achieved at $x = 1$ during one complete period for a water micropump with $L = 1$ mm, $a = 10\ \mu$m, $d = 75\ \mu$m, $\rho = 10^3$ kg/m^3, $\nu = 10^{-6}$ m^2/s, $\rho_A = 2.336 \times 10^3$ kg/m^3, $E = 10^{11}$ N/m^2, $p_A = 30.8N^2$, $N = 100$, and an excitation frequency of 400 Hz. The comparison between the numerical results is given by 2D and 3D models.

Hence we obtain, as 3D model equations for the two-layer geometry presented in Fig. 4,

$$\frac{\partial^2 \eta}{\partial t^2} + \alpha \frac{\partial^4 \eta}{\partial x^4} = -\beta(p_A - \Delta P), \tag{29}$$

$$\frac{\partial \eta}{\partial t} = -\frac{\partial}{\partial x}\left(\frac{q}{\delta_y}\right), \tag{30}$$

$$\frac{\partial(\Delta p)}{\partial x} = -\frac{\partial}{\partial t}\left(\frac{q}{\delta_y}\right)\left(\frac{1}{1+\eta} + \frac{1}{1-\eta}\right) - 12\frac{q}{\delta_y}\left[\frac{1}{(1+\eta)^3} + \frac{1}{(1-\eta)^3} + \frac{\delta^2}{\delta_y^2}\frac{1}{1+\eta} + \frac{\delta^2}{\delta_y^2}\frac{1}{1-\eta}\right], \tag{31}$$

with the boundary conditions $\eta(t, x = 0) = \eta(t, x = 1) = \partial\eta/\partial x|_{x=0} = \partial\eta/\partial x|_{x=1} = 0$, $q(t, x = 0) = 0$, and $\Delta P(t, x = 1) = 0$. The linear stability analysis for the case without driving $p_A = 0$ in the above system of equations shows the same result as in Sec. II A: The fixed point $\eta^{(0)} = q^{(0)} = p^{(0)} = 0$ is linearly stable for all k.

B. Closed geometry

For the water pump with the parameters indicated in Sec. II B (with $d = 75\ \mu$m for the water film thicknesses in the lower and the upper layer), Fig. 5 plots the pressure drop $\Delta P = p_1 - p_2$ in the middle of the pump channel on the maximal flow rate q, achieved at $x = 1$, for two depths of the pump channel: $b \gg 75\ \mu$m ($\delta/\delta_y \ll 1$, i.e., in the limit of the 2D model) and $b = 75\ \mu$m ($\delta/\delta_y = 1$, in the limit of the 3D model) during one complete period. Figure 5 shows positive and negative flow rates inside the channel and a symmetrical behavior around $q = 0$: The liquid is pumped from the lower to the upper side and vice versa. For $\delta/\delta_y = 1$, the pressure drop ΔP in the 3D model is two times larger than in the 2D description. For $\delta/\delta_y = 1$, the viscous diffusion in the transversal direction becomes stronger and we need a larger ΔP to cover the losses through diffusion.

For the parameters considered until now, $\eta_{\max}/d < 0.01 \ll 1$, which explains the linear dependence shown by Fig. 5. Now we consider an ethanol pump with a silicon elastic beam having

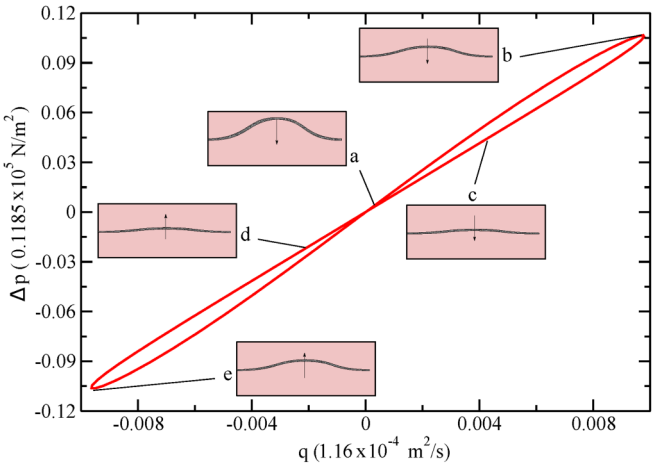

FIG. 6. Same as in Fig. 5 in the frame of the 2D model for an ethanol micropump with $L = 2.294$ mm, $a = 29$ μm, $d = 30$ μm, $\rho = 790$ kg/m^3, $\nu = 1.52 \times 10^{-6}$ m^2/s, $\rho_A = 2.336 \times 10^3$ kg/m^3, $E = 10^{11}$ N/m^2, $p_A = 0.095N^2$, $N = 100$, and an excitation frequency of 34 Hz. Insets a–e show the beam position at different times during one complete period.

the parameters $L = 2.294$ mm, $a = 29$ μm, $d = 30$ μm, $\rho = 790$ kg/m^3, $\nu = 1.52 \times 10^{-6}$ m^2/s, $\rho_A = 2.336 \times 10^3$ kg/m^3, and $E = 10^{11}$ N/m^2. For this case, the model parameters are $\alpha = 38$ and $\beta = 2 \times 10^3$. For actuating forces $p_A \cos^2(2\pi f t)$ with the excitation frequency $2f = 34$ Hz and $p_A = 0.095N^2$ ($N = 100$), one achieves, for the maximal deformation in the string, $\tilde{\eta}_{\max} = 9.2$ μm, almost 30% from the liquid thickness $d = 30$ μm. For this case, we obtain, during one complete period, the representation shown by Fig. 6, which emphasizes in the insets the beam positions at different times during one complete period. Two- and three-dimensional results for the ethanol pump with $b \gg 30$ μm ($\delta/\delta_y \ll 1$) and $b = 30$ μm ($\delta/\delta_y = 1$) are presented in Fig. 7. By comparing the

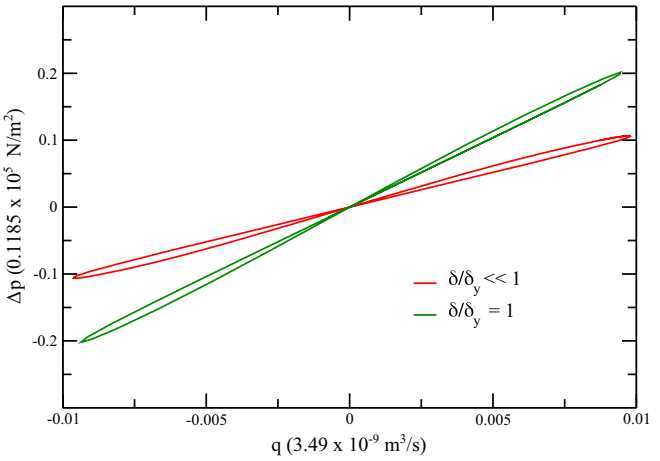

FIG. 7. Pressure difference $\Delta P = p_1 - p_2$ in the middle of the channel versus flow rate q achieved at $x = 1$ during one complete period for an ethanol micropump with $L = 2.294$ mm, $a = 29$ μm, $d = 30$ μm, $\rho = 790$ kg/m^3, $\nu = 1.52 \times 10^{-6}$ m^2/s, $\rho_A = 2.336 \times 10^3$ kg/m^3, $E = 10^{11}$ N/m^2, $p_A = 0.095N^2$, $N = 100$, and an excitation frequency of 34 Hz. The comparison between the numerical results is given by 2D and 3D models.

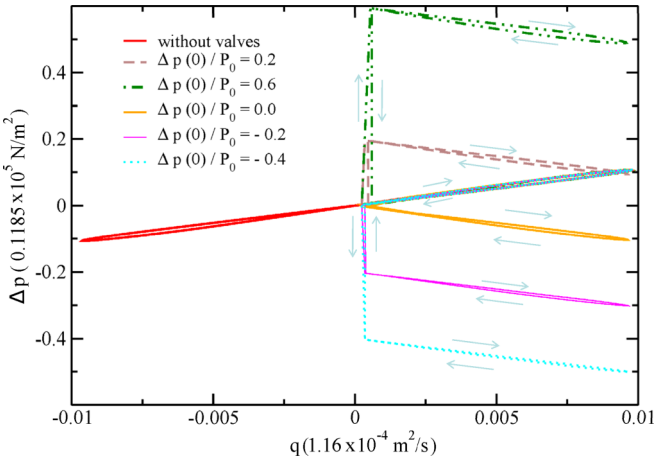

FIG. 8. Same as Fig. 5 for the two-layer micropump with the boundary conditions explained in Sec. III C in the two-dimensional model and for different counterpressures $-\Delta P(0)$. The other parameters are $L = 2.294$ mm, $a = 29\ \mu$m, $d = 30\ \mu$m, $\rho = 790$ kg/m^3, $\nu = 1.52 \times 10^{-6}$ m^2/s, $\rho_A = 2.336 \times 10^3$ kg/m^3, $E = 10^{11}$ N/m^2, $p_A = 0.095N^2P_0$, $N = 100$, $P_0 = 0.1185 \times 10^5$N/m^2, and an excitation frequency of 34 Hz.

maxima of the flow rates from Figs. 5 and 7, we can see that the flow rate in the water pump is one order of magnitude larger than in the ethanol pump.

C. Implementation of the valves: Ratchet systems

For the remaining paper we work in the frame of the 2D model ($\delta/\delta_y \ll 1$) with the parameters of the two-layer ethanol pump with a silicon elastic beam with the parameters mentioned in the preceding section. The valves are incorporated with the help of the boundary conditions. Three ideal valves are implemented on the liquid pump depicted in Fig. 4: two on the left lateral wall in the upper and the lower layer and the third one between the elastic beam and the right lateral wall. Thus, the pump works in two cycles: During the first half cycle [Fig. 4(b)], the valves on the left lateral walls are closed, the internal valve is open, and the beam moves from the maximal deflected position to the horizontal position (see insets a–c in Fig. 6). For this half cycle, one applies the boundary conditions

$$q(t, x = 0) = 0, \quad \Delta P(t, x = 1) = 0.$$

For the second half cycle [Fig. 4(c)], the lateral valves are open, the internal valve is closed, and the beam is actuated from the horizontal position in the upper direction until its maximal deformation is reached. Now we apply the boundary conditions

$$\Delta P(t, x = 0) = \Delta P(0), \quad q(t, x = 1) = 0,$$

with $\Delta P(0)$ an input parameter that is negative for the pump regime.

In this way we realize the flow only in one direction inside the pump (only positive flow rates), creating in this way a ratchet system (Fig. 8). The transition jumps from the first half-time to the second half-time (i.e., to the working time of the pump) from Fig. 8 become stronger with the increase of the counterpressure $-\Delta P(0)$.

The averaged flow rate $\bar{q}$ along the x direction on the second half-time of the micropump (during the working time) has been plotted for two excitation frequencies. The curves plotted in Fig. 9 show an almost linearly monotonic decrease with the counterpressure $-\Delta P(0)$ (characteristic for pumps [42]), steeper at higher excitation frequency. Indeed, the flow rate is increasing to the forcing frequency because the volume displaced by each pump stroke is delivered more often. Multiplying the values from the ordinate in Fig. 9 with the ethanol density, with the width (depth) of the pump

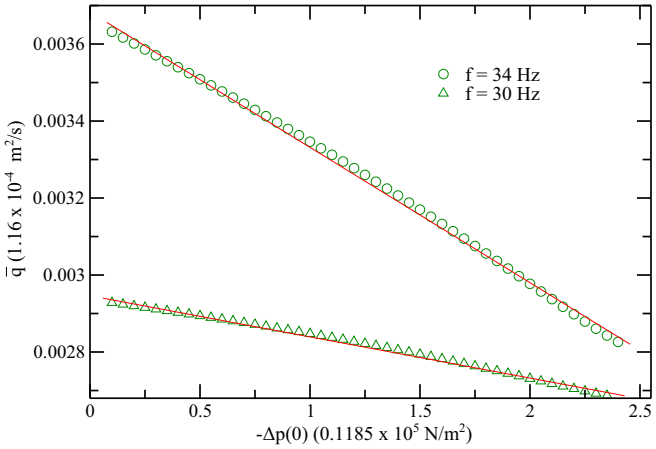

FIG. 9. Averaged flow rate $\bar{q}$ versus counterpressure $-\Delta P^{(0)}$ for an ethanol micropump in two-layer geometry with $L = 2.294$ mm, $a = 29$ μm, $d = 30$ μm, $\rho = 790$ kg/m^3, $\nu = 1.52 \times 10^{-6}$ m^2/s, $\rho_A = 2.336 \times 10^3$ kg/m^3, and $E = 10^{11}$ N/m^2. The average has been done in the x direction and during the second half-time of the micropump.

channel, and with the factor 2 (in the first half-time of the cycle the lateral valves communicating with the external reservoirs are closed), we can calculate the mass of ethanol per unit volume evacuated per cycle by the two-layer pump sketched in Fig. 4.

D. Porous beam

We assume now that the elastic beam in Fig. 4 is porous (with the permeability K), simulating leakage. The kinematic boundary condition (13) is extended to

$$\frac{\partial \eta}{\partial t} = -\frac{\partial q}{\partial x} - \frac{K}{\rho \nu}(p_1 - p_2) \tag{32}$$

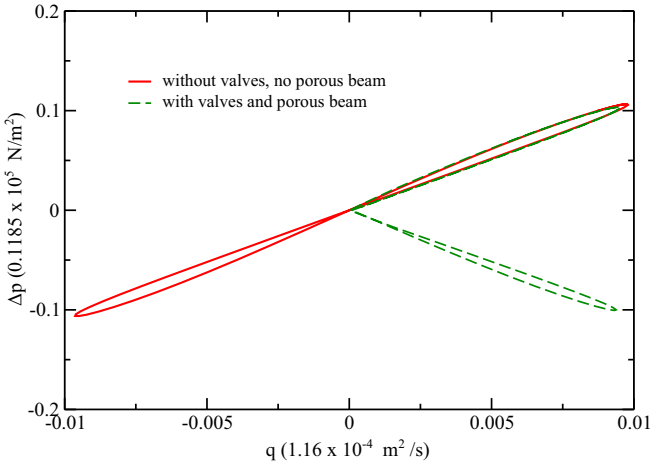

FIG. 10. Same as Fig. 5 for a porous elastic beam with $K = 0.17 \times 10^{-12}$ m. The other parameters are $L = 2.294$ mm, $a = 29$ μm, $d = 30$ μm, $\rho = 790$ kg/m^3, $\nu = 1.52 \times 10^{-6}$ m^2/s, $\rho_A = 2.336 \times 10^3$ kg/m^3, $E = 10^{11}$ N/m^2, and $\Delta P(0) = 0$.

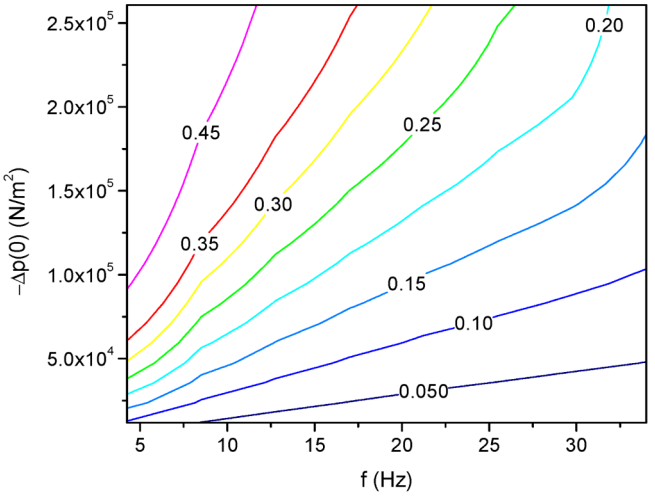

(a)

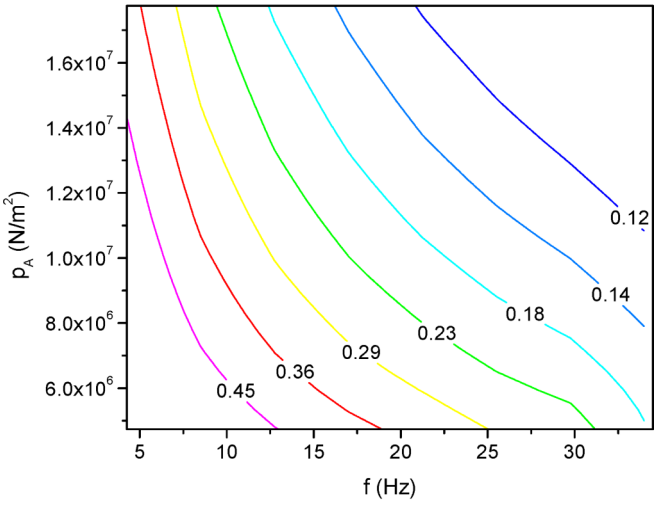

(b)

FIG. 11. Efficiency of the ethanol micropump designed in Fig. 4 for $L = 2.294$ mm, $a = 29\ \mu$m, $d = 30\ \mu$m, $\rho = 790$ kg/m^3, $\nu = 1.52 \times 10^{-6}$ m^2/s, $\rho_A = 2.336 \times 10^3$ kg/m^3, and $E = 10^{11}$ N/m^2. The contour lines of the efficiency are plotted as a function of (a) the counterpressure $-\Delta P(0)$ and the excitation frequency (with $p_A = 0.095 N^2 P_0$, $N = 100$, and $P_0 = 0.1185 \times 10^5$N/m^2) and (b) the actuated pressure p_A and the excitation frequency [with $-\Delta P(0) = P_0$].

(Darcy's law). The presence of the porosity decreases the flow rates (Fig. 10). For $K = 0.17 \times 10^{-12}$ m, our two-dimensional simulations reveal a 4% decrease of the maximal flow rate (from 1.14×10^{-6} m^2/s to 1.1×10^{-6} m^2/s) for the ethanol two-layer micropump. Higher permeabilities in the system will lead to lower flow rates.

E. Efficiency of a micropump

For the pump geometry depicted in Fig. 4, the only dissipation mechanism is the shearing friction inside the fluid. From hydrodynamic considerations, the energy dissipation due to frictional forces

inside the fluid per unit time is

$$\dot{W}_D = \rho\nu \int_0^L \int_0^h v_x \frac{\partial^2 v_x}{\partial z^2} dz\, dx. \tag{33}$$

From the derivation of the lubrication model (Sec. II A) we have

$$v_x = \frac{6q}{h^3} z(h - z)$$

and

$$\frac{\partial^2 v_x}{\partial z^2} = -\frac{12q}{h^3}.$$

According to the scaling introduced in Sec. II A, we obtain, for the energy dissipated along the pump channel per unit time,

$$\dot{W}_D = -12 \int_0^L \int_0^h v_x \frac{q}{h^3} dz\, dx = -12 \int_0^L \frac{q^2}{h^3} dx. \tag{34}$$

We define the efficiency $\mathcal{E}$ of the micropump

$$\mathcal{E} = \frac{W_{\text{liq}}}{W_{\text{liq}} + |W_D|}, \tag{35}$$

where W_{liq} represents the liquid work performed in the second half cycle

$$W_{\text{liq}} = \int_{\text{2nd half-time}} [-\Delta P(0)] q(0) dt,$$

with $-\Delta P(0)$, $q(0)$ calculated at $x = 0$, and the dissipated energy (as an absolute value) evaluated over the second half of the micropump

$$|W_D| = \int_{\text{2nd half-time}} |\dot{W}_D| dt.$$

The diagrams plotted in Fig. 11 show contour lines of the efficiency as a function of the counterpressure $-\Delta P(0)$, the excitation frequency, and the pressure at the actuator p_A. The pump efficiency increases with the increase of the counterpressure $-\Delta P(0)$ and decreases with the increase of the excitation frequency or the actuated pressure p_A, when the viscous friction inside the fluid becomes higher. For excitation frequencies varying between 10 and 20 Hz, $p_A = 0.095 N^2 P_0$, $N = 100$, $P_0 = 0.1185 \times 10^5 \text{N/m}^2$, and counterpressures $-\Delta P(0)$ between 10^5 and $2 \times 10^5 \text{N/m}^2$, the efficiencies of the liquid pump depicted in Fig. 4, with the parameters mentioned in Sec. III B, are in the same range as those calculated for a water pump by air lift [43] for water temperatures between 30° and 60°.

IV. CONCLUSION

We have developed a lubrication theory for two pump geometries: a single thin liquid layer actuated by a periodic force at the elastic beam and a two-layer geometry actuated by an elastic beam. For the second geometry, the beam actuates the liquid from both sides. The Euler-Bernoulli equation for transverse deformations of an elastic beam has been coupled to the fundamental hydrodynamic equations: the Navier-Stokes equation and the continuity equation in the long-wave approximation. In this way, we connect the transverse displacement of the beam with hydrodynamic quantities (pressure, velocity fields, and flow rates). Appropriate boundary conditions incorporate the function of the valves. Easy to implement, convenient and suitable for time-consuming problems (even in three spatial dimensions), the derived lubrication model is very attractive not only for the fundamental

research. This tool can also become a competitive engineering software for useful applications in micromachinery.

The derivation of the theoretical model was followed by numerical simulations. Thus, we have estimated flow rates (in two and three spatial dimensions) for different system parameters and we have shown how to consider a porous elastic beam (simulating leakage) and how to compute the efficiency of a well-designed liquid pump.

ACKNOWLEDGMENTS

This research was part of the NED-VAMP Project "Nano Electrostatic Drive—Valves and Micropumps" (Grant No. 85004248) and was cofinanced by the European Fond for Regional Developments.

[1] E. Bertrand, D. Bonn, D. Broseta, J. O. Indekeu, J. Meunier, K. Ragil, and N. Shahidzadeh, Wetting of alkanes on water, J. Petrol. Sci. Eng. **33**, 217 (2002).

[2] N. Kapur and P. H. Gaskell, Morphology and dynamics of droplet coalescence on a surface, Phys. Rev. E **75**, 056315 (2007).

[3] G. F. Christopher, J. Bergstein, N. B. End, M. Poon, N. Nguyen, and S. L. Anna, Coalescence and splitting of confined droplets at microfluidic junctions, Lab Chip **9**, 1102 (2009).

[4] L. A. Riolfo, Y. Nagatsu, S. Iwata, R. Maes, P. M. J. Trevelyan, and A. De Wit, Experimental evidence of reaction-driven miscible viscous fingering, Phys. Rev. E **85**, 015304 (2012).

[5] D. N. Pagonis, A. Petropoulos, and G. Kaltsas, A pumping actuator implemented on a PCB substrate by employing water electrolysis, Microelectron. Eng. **95**, 65 (2012).

[6] B. Liu, Y. Hou, D. Li, and J. Yang, A thermal bubble micro-actuator with induction heating, Sensor. Actuat. A **222**, 8 (2015).

[7] P.-J. Peng and Y.-C. Su, Preprogrammed, rate-switchable osmotic pumping on a chip, Microfluid. Nanofluid. **18**, 267 (2015).

[8] M. Sheikhlou, R. Shabani, and G. Rezazadeh, Nonlinear analysis of electrostatically actuated diaphragm-type micropumps, Nonlinear Dyn. **83**, 951 (2016).

[9] D. Panescu, MEMS in medicine and biology, IEEE Eng. Med. Biol. Mag. **25**, 19 (2006).

[10] A. Oron, S. H. Davis, and S. G. Bankoff, Long-scale evolution of thin liquid films, Rev. Mod. Phys. **69**, 931 (1997).

[11] R. V. Craster and O. K. Matar, Dynamics and stability of thin liquid films, Rev. Mod. Phys. **81**, 1131 (2009).

[12] S. J. Vanhook, M. F. Schatz, J. B. Swift, W. D. McCormick, and H. L. Swinney, Long-wavelength surface-tension-driven Bénard convection: Experiment and theory, J. Fluid Mech. **345**, 45 (1997).

[13] A. Oron, Nonlinear dynamics of three-dimensional long-wave Marangoni instability in thin liquid films, Phys. Fluids **12**, 1633 (2000).

[14] M. Bestehorn and K. Neuffer, Surface Patterns of Laterally Extended Thin Liquid Films in Three Dimensions, Phys. Rev. Lett. **87**, 046101 (2001).

[15] M. Bestehorn, A. Pototsky, and U. Thiele, 3D Large scale Marangoni convection in liquid films, Eur. Phys. J. B **33**, 457 (2003).

[16] U. Thiele, M. G. Velarde, K. Neuffer, M. Bestehorn, and Y. Pomeau, Sliding drops in the diffuse interface model coupled to hydrodynamics, Phys. Rev. E **64**, 061601 (2001).

[17] U. Thiele and E. Knobloch, Thin liquid films on a slightly inclined heated plate, Physica D **190**, 213 (2004).

[18] U. Thiele and E. Knobloch, On the depinning of a driven drop on a heterogeneous substrate, New J. Phys. **8**, 313 (2006).

[19] J. A. Diez, A. G. Gonzales, and L. Kondic, On the breakup of fluid rivulets, Phys. Fluids **21**, 082105 (2009).

[20] P. Beltrame, E. Knobloch, P. Hanggi, and U. Thiele, Rayleigh and depinning instabilities of forced liquid ridges on heterogeneous substrates, Phys. Rev. E **83**, 016305 (2011).
[21] N. Clarke, Instabilities in thin-film binary mixtures, Eur. Phys. J. E **14**, 207 (2004).
[22] O. K. Matar, R. V. Craster, and K. Sefiane, Dynamic spreading of droplets containing nanoparticles, Phys. Rev. E **76**, 056315 (2007).
[23] L. O. Naraigh and J. L. Thiffeult, Nonlinear dynamics of phase separation in thin films, Nonlinearity **23**, 1559 (2010).
[24] M. Bestehorn and I. D. Borcia, Thin film lubrication dynamics of a binary mixture: Example of an oscillatory instability, Phys. Fluids **22**, 104102 (2010).
[25] U. Thiele, Note on thin film equations for solutions and suspensions, Eur. Phys. J. Spec. Top. **197**, 213 (2011).
[26] L. Frastia, A. J. Archer, and U. Thiele, Dynamical Model for the Formation of Patterned Deposits at Receding Contact Lines, Phys. Rev. Lett. **106**, 077801 (2011).
[27] R. Borcia, S. Menzel, M. Bestehorn, S. Karpitschka, and H. Riegler, Delayed coalescence of droplets with miscible liquids: Lubrication and phase field theories, Eur. Phys. J. E **34**, 24 (2011).
[28] R. Borcia, I. D. Borcia, and M. Bestehorn, Nonlinear dynamics of thin liquid films consisting of two miscible components, Phys. Rev. E **86**, 056319 (2012).
[29] K. John, P. Hanggi, and U. Thiele, Ratchet-driven fluid transport in bounded two-layer films of immiscible liquids, Soft Matter **4**, 1183 (2008).
[30] K. John and U. Thiele, Self-Ratcheting Stokes Drops Driven by Oblique Vibrations, Phys. Rev. Lett. **104**, 107801 (2010).
[31] N. O. Rojas, M. Argentina, E. Cerda, and E. Tirapegui, Inertial Lubrication Theory, Phys. Rev. Lett. **104**, 187801 (2010).
[32] E. S. Benilov and J. Billingham, Drops climbing uphill on an oscillating substrate, J. Fluid Mech. **674**, 93 (2011).
[33] M. Bestehorn, Q. Han, and A. Oron, Nonlinear pattern formation in thin liquid films under external vibrations, Phys. Rev. E **88**, 023025 (2013).
[34] M. Bestehorn, Laterally extended thin liquid films with inertia under external vibrations, Phys. Fluids **25**, 114106 (2013).
[35] A. Pototsky and M. Bestehorn, Faraday instability of a two-layer liquid film with a free upper surface, Phys. Rev. Fluids **1**, 023901 (2016).
[36] M. Bestehorn and A. Pototsky, Faraday instability and nonlinear pattern formation of a two-layer system: A reduced model, Phys. Rev. Fluids **1**, 063905 (2016).
[37] W. F. Riley and L. W. Zachary, *Introduction to Mechanics of Materials* (Wiley, New York, 1989), pp. 288 and 508.
[38] A. A. Shabana, *Theory of Vibration. Vol. II: Discrete and Continuous Systems* (Springer, New York, 1991), p. 216.
[39] C. Hirsch, *Numerical Computation of Internal and External Flows* (Wiley, New York, 1998), Vol. 1, p. 201.
[40] M. Bestehorn, *Hydrodynamik und Strukturbildung* (Springer, Berlin, 2006), p. 347.
[41] M. Bestehorn, *Computational Physics* (de Gruyter GmbH, Berlin, 2016), p. 121.
[42] W. K. Schomburg, *Introduction to Microsystem Design* (Springer, Berlin, 2011), p. 242.
[43] A. Oueslati, A. Hannachi, and M. Elmaaoui, Effect of air humidification on the pumping efficiency of water in a packed column humidifier, Energy Proced. **74**, 1381 (2015).

Correction: Minor errors in Eqs. (28) and (31) have been fixed.